HyperScience International Journal

Original Research Papers
Open Access Journals
ISSN: 2821-3300

HIJ, Vol 6, No 3, pp 46-61, Sep 2026
https://doi.org/10.55672/hij2026pp46-61


# A Navier-Stokes-Based Validity Framework for Linear and Nonlinear Transient Pressure-Wave Modeling in Spacecraft Pumped-Fluid Loops

**Misha Nikouravan**

*Mechanical Engineering, CentraleSupélec, Université Paris-Saclay, France*

*Received: May 2026*
*Received in revised form: Aug 2026*
*Published: Sep 2026*

## ABSTRACT

Transient pressure disturbances in spacecraft pumped-fluid loops are commonly represented by linearized one-dimensional models, yet the error introduced by linearization is rarely quantified against a nonlinear formulation derived from the same conservation laws. This study develops a Navier-Stokes-based validity framework for single-phase spacecraft pumped-fluid loops. Mass conservation and axial momentum balance for a slightly compressible Newtonian liquid are reduced to coupled pressure-velocity equations that retain convective inertia and flow-regime-dependent wall friction. A consistent linear model is obtained by perturbation about a nonzero steady circulation state. The equations are solved with fourth-order spatial differencing and classical fourth-order Runge-Kutta integration. Verification against an exact smooth nonlinear characteristic solution gives the designed fourth-order convergence, with relative error decreasing to $2.72\times10^{-10}$ at 800 grid points, and the nonlinear solution recovers the moving-base linear limit as the acoustic Mach number tends to zero. Two spacecraft-informed applications are examined: a turbulent HFE-7200 external thermal-control loop and a laminar 50/50 propylene-glycol/water internal loop. For a 20% smooth pump disturbance, the global linear-versus-nonlinear pressure discrepancies are 0.0667% and 0.0116%, respectively, with peak transient pressure excursions of approximately 74.8 and 13.6 kPa. Even at the largest tested disturbance amplitude (45%), the discrepancies remain 0.1481% and 0.0260%. A broader dimensionless map shows that errors above 1% require simultaneously larger acoustic Mach number and disturbance amplitude, while the 5% threshold in the tested turbulent family appears only near $M \gtrsim 0.08$ with strong forcing. The results show that the consistent linear model is quantitatively sufficient for the representative low-Mach spacecraft loops studied, while the nonlinear formulation provides a verified criterion for identifying conditions under which that simplification ceases to be adequate.

**Keywords:** Navier-Stokes equations; hydraulic transients; pressure waves; model validity; nonlinear fluid dynamics; spacecraft thermal control; mechanically pumped fluid loop.



## 1. INTRODUCTION

Thermal management is a fundamental spacecraft design function because onboard electronics, payloads, power systems, and crew-support hardware must operate within limited temperature ranges while heat is ultimately rejected to space by radiation. Modern reviews emphasize that increasing heat loads and distributed high-power equipment are strengthening the need for efficient heat acquisition, transport, and rejection technologies [1,2]. Mechanically pumped fluid loops (MPFLs) are particularly attractive when heat must be transported over appreciable distances or collected from several locations, because a circulating liquid can couple distributed cold plates or heat exchangers to remote radiators with controllable flow and substantial thermal capacity [1,2].

Single-phase MPFLs have a long spacecraft heritage and remain relevant for active thermal-control architectures. Their behavior is governed not only by steady heat-transfer requirements but also by hydraulic transients generated by pump-speed changes, valve motion, flow redistribution, start-up, shutdown, and changes in system resistance.

Transient simulation and experimental correlation of an actively controlled single-phase spacecraft MPFL have previously been reported [3], while later work has investigated component-level control and thermal response within single-phase spacecraft loops [4].

More recently, high-fidelity thermohydraulic and model-data hybrid approaches have been applied to operational space-station fluid loops, illustrating the continuing importance of first-principles mass, momentum, and energy conservation in spacecraft thermal-system analysis [5].

From the fluid-mechanics perspective, a rapid change in flow produces pressure disturbances that propagate through a confined liquid at a finite wave speed determined by fluid compressibility and conduit compliance. Classical one-dimensional hydraulic-transient models provide an efficient description of this process and remain central to engineering pressure-surge analysis.

However, conventional formulations frequently employ linearizing assumptions, including small fluid velocity relative to wave speed and simplified representations of wall friction. Contemporary reviews of water-hammer modeling show that one-dimensional approaches remain valuable, while also documenting the additional physics captured by higher-fidelity formulations [6].

Pressure-wave attenuation can arise from several mechanisms, including skin friction, fluid-structure effects, and other dissipative processes, and the interpretation of measured damping therefore requires care [7]. The distinction between linear and nonlinear modeling becomes especially important when a transient is superposed on a nonzero circulating base flow. Convective acceleration is intrinsically nonlinear, while commonly used Darcy-Weisbach-type resistance introduces an additional velocity-dependent nonlinearity in turbulent conditions. At the same time, the wall shear stress during a sufficiently rapid transient can depart from its quasi-steady value. Extensive pipe-flow research has therefore developed unsteady-friction models and clarified the limitations of purely quasi-steady resistance formulations [8,9].

These observations imply that a low acoustic Mach number alone does not automatically guarantee that every nonlinear or transient-resistance contribution is negligible; the adequacy of linearization must be evaluated against the relevant flow regime, disturbance amplitude, geometry, and time scale.

Spacecraft-loop studies have primarily focused on thermal architecture, component performance, system control, or high-fidelity thermohydraulic prediction [3,4,5], whereas the hydraulic-transient literature has developed increasingly sophisticated treatments of pressure-wave propagation and friction [6,7,8,9].

This leaves a useful modeling question at their intersection: for a single-phase spacecraft pumped-fluid loop operating about a steady circulation state, when does a linear transient model remain sufficiently accurate, and when do nonlinear corrections become large enough to justify the additional mathematical and computational complexity?

Answering this question requires a comparison in which the linear and nonlinear systems are derived from the same conservation laws, use consistent base states and boundary conditions, and are evaluated using quantitative error measures rather than qualitative curve comparisons. Accordingly, the aim of the present study is to develop and test a Navier-Stokes-based validity framework for linear and nonlinear reduced-order transient models of single-phase spacecraft pumped-fluid loops. The study

**(i)** derives coupled pressure-velocity equations from mass conservation and axial momentum balance for a slightly compressible Newtonian liquid;

**(ii)** separates convective and frictional sources of nonlinearity;

**(iii)** obtains the consistent linear perturbation model about a moving base flow;

**(iv)** verifies the numerical solution through limiting-case and grid-convergence tests; and

**(v)** constructs a parameter-based validity map using representative spacecraft thermal-control conditions.

The intended contribution is therefore not a claim that the underlying nonlinear pipe-flow equations are new, but a quantitative criterion for selecting an appropriate level of model complexity for spacecraft pumped-fluid transients. This scope also permits a scientifically meaningful outcome if the linear model proves adequate over part of the practical operating envelope.

## 2. PHYSICAL MODEL AND GOVERNING EQUATIONS

### 2.1. Closed-loop idealization and dependent variables

The spacecraft fluid system is represented by a single-phase liquid circulating through a slender closed conduit of total hydraulic length $L$ and representative internal diameter $D$. The axial coordinate $x$ follows the loop centerline, while $u(x,t)$, $p(x,t)$, and $\rho(x,t)$ denote the cross-sectionally averaged axial velocity, pressure, and density, respectively.

This one-dimensional representation is appropriate when axial length scales substantially exceed the conduit diameter and when the quantities of interest are the propagating hydraulic transients rather than detailed local three-dimensional fields [6,10,11].

Localized devices such as the pump, valves, heat exchangers, bends, and accumulators are not discarded; their hydraulic action will be introduced later through localized source or boundary relations, while the present section establishes the governing equations for the intervening fluid segments.

A nonzero steady circulation speed $U_0$ is allowed. This point is essential because the eventual linear model must be obtained by perturbing the same governing equations about the moving base state, rather than by replacing the system with a zero-flow acoustic equation. Recent transient-pipe studies likewise emphasize that the nonlinear convective terms are present in the governing equations even though they are commonly neglected in classical low-Mach water-hammer approximations [10,12].

### 2.2. Baseline modeling assumptions

The baseline assumptions are summarized in Table 1. They define the intended range of the reduced-order model; assumptions that depend on the final spacecraft operating point, particularly single-phase behavior and the adequacy of quasi-steady friction, will be checked again during the application stage.

**Table 1.** Baseline assumptions for the reduced-order spacecraft-loop model.

| Assumption | Baseline choice | Model implication / check |
|---|---|---|
| **Fluid constitution** | Single-phase Newtonian liquid | Appropriate for the baseline PGW/HFE-type spacecraft coolant cases; phase change and gas entrainment is excluded. |
| **Dimensional reduction** | Quasi-one-dimensional, cross-sectionally averaged flow | Retains axial pressure-wave propagation while omitting local secondary-flow detail. |
| **Compressibility and wall response** | Slight liquid compressibility and small conduit distensibility represented by an effective wave celerity c | Allows finite-speed pressure waves without solving a separate structural PDE in the baseline model. |
| **Fluid properties** | ρ, μ, and the reference c are treated as constant within each short transient case | Temperature dependence is deferred to a later extension and checked against the selected operating range. |
| **Body force** | Axial gravitational/body-force contribution is neglected in the baseline microgravity case | Appropriate for the nominal orbital spacecraft application; sustained vehicle acceleration would require restoring this term. |
| **Wall friction** | Quasi-steady Darcy-Weisbach resistance is the baseline closure | Adequate for the first validity map; very rapid transients may require an unsteady-friction correction. |
| **Phase integrity** | No cavitation, boiling, or two-phase transition | Must be verified a posteriori by the minimum pressure and operating temperature in each application. |
| **Thermal coupling** | Hydraulic transient solved without a simultaneous energy equation | Justified when the pressure-wave time scale is short compared with the dominant thermal time scale. |
| **Loop components** | Pump/valve actions are treated as localized hydraulic elements | Prevents artificial distributed forcing and preserves the conservation-law form in ordinary pipe segments. |

### 2.3. Conservation of mass and momentum

The derivation begins with the local conservation laws rather than with an assumed pressure-wave equation. For a compressible continuum, conservation of mass is

$$\frac{\partial \rho}{\partial t} + \nabla \cdot (\rho u) = 0 \tag{1}$$

where the bold velocity vector denotes the three-dimensional continuum field. For a Newtonian fluid with constant dynamic viscosity in the baseline derivation, the momentum equation can be written as

$$\rho \left[\frac{\partial u}{\partial t} + (\boldsymbol{u} \cdot \nabla)\boldsymbol{u}\right] = -\nabla p + \mu \nabla^2 \boldsymbol{u} + \rho \boldsymbol{b} \tag{2}$$

where $\mu$ is the dynamic viscosity and $\boldsymbol{b}$ is body acceleration. Equations (1) and (2) provide the fundamental mass and momentum basis of the reduced model. The assumptions in Table 1 are applied only after these conservation laws have been stated, which makes clear which physical terms are retained and which are neglected.

### 2.4. One-dimensional pressure-velocity form

Let $A(p)$ denote the local conduit cross-sectional area. Integrating mass conservation over the cross-section gives the quasi-one-dimensional continuity equation

$$\frac{\partial(\rho A)}{\partial t} + \frac{\partial(\rho A u)}{\partial x} = 0 \tag{3}$$

The pressure dependence of liquid density and the small elastic area change of the conduit can be combined into an effective pressure-wave celerity. If $K$ is the liquid bulk modulus, the local compliance may be represented in differential form by

$$\frac{1}{\rho c^2} = \frac{1}{K} + \frac{1}{A}\frac{\mathrm{d}A}{\mathrm{d}p} \tag{4}$$

so that the rigid-wall limit is recovered when $dA/dp = 0$. This effective-celerity treatment is standard in one-dimensional hydraulic-transient theory, while more complete fluid-structure interaction models retain additional structural degrees of freedom [10,11]. Substitution of Eq. (4) into Eq. (3) gives the pressure form

$$\frac{\partial p}{\partial t} + u\frac{\partial p}{\partial x} + \rho c^2 \frac{\partial u}{\partial x} = 0 \tag{5}$$

The first two terms in Eq. (5) form the material pressure derivative; the term $u\partial p/\partial x$ is therefore a convective contribution that disappears from the conventional zero-advection linear wave model. Cross-sectional averaging of the axial momentum balance, neglecting the baseline body-force contribution and representing wall resistance by a Darcy-Weisbach closure, gives

$$\frac{\partial u}{\partial t} + u\frac{\partial u}{\partial x} + \frac{1}{\rho}\frac{\partial p}{\partial x} + \frac{f_D}{2D}u|u| = 0 \tag{6}$$

where $f_D$ is the Darcy friction factor. Equation (6) retains both the convective acceleration $u\partial u/\partial x$ and the velocity-dependent friction term. Similar nonlinear one-dimensional transient equations are established in the modern hydraulic-transient literature [10,12], so the contribution of the present study is not the existence of these terms but their consistent spacecraft-loop linearization and quantitative validity assessment. The instantaneous Reynolds number used to distinguish viscous-flow regimes is

$$R_e = \frac{\rho|u|D}{\mu} \tag{7}$$

For fully developed laminar flow, $f_D = 64/Re$, which makes the corresponding Darcy resistance proportional to velocity. In turbulent flow the quadratic factor $u|u|$ remains an important nonlinear contribution, with the friction factor additionally depending on Reynolds number and wall roughness. For sufficiently rapid transients, however, wall shear can lag the instantaneous mean flow and a quasi-steady friction closure may underpredict or misrepresent damping; this limitation is well documented in unsteady-friction studies [7,8,9].

The baseline model will therefore be applied to finite-time pump/flow disturbances rather than an idealized instantaneous valve slam, and the characteristic transient time will later be checked against this assumption. Equations (5)-(7), together with the effective celerity relation (4), form the physical foundation for the steady-base perturbation formulation developed in Section 3, where convective and frictional nonlinearities are separated and consistent linear and nonlinear reduced-order systems are obtained.

## 3. STEADY-BASE PERTURBATION FORMULATION AND LINEARIZATION

### 3.1. Moving base state and dimensionless perturbations

The transient comparison must be made about the same nonzero circulation state in both models. Let $U_0 > 0$ denote the reference steady loop velocity and let $\bar{p}(x)$ denote the corresponding steady pressure profile. The instantaneous fields are decomposed into a steady component and a transient perturbation, while length and time are scaled with the loop length and acoustic travel time:

$$u = U_0(1+V), \quad p = \bar{p} + \rho c U_0 P, \quad X = \frac{x}{L}, \quad \tau = \frac{ct}{L} \tag{8}$$

Here $V(X,\tau)$ is the velocity perturbation relative to $U_0$, and $P(X,\tau)$ is the pressure perturbation scaled by the classical acoustic pressure scale $\rho c U_0$. The baseline calculations are restricted to $V > -1$ so that the mean flow does not reverse. Flow reversal can be handled by the original absolute-value friction law, but the local linearization would then be piecewise and is not required for the present validity map. Two dimensionless groups appear naturally: the acoustic Mach number $M$ and the turbulent quasi-steady friction parameter $\Gamma$. For a reference Darcy factor $f_0$ they are

$$M = \frac{U_0}{c}, \qquad \Gamma = \frac{f_0 L}{2D}M \tag{9}$$

The steady pressure gradient in a closed pumped loop produces only a small density variation when the liquid is slightly compressible. In the present perturbation reduction, terms generated by convection of that steady pressure gradient are higher order, with the representative scale

$$\varepsilon_b = \frac{f_0 L}{2D}M^2 = \Gamma M \tag{10}$$

and are neglected when $\varepsilon_b \ll 1$. This condition will be evaluated explicitly for the spacecraft parameter sets rather than assumed without checking. The resulting formulation is therefore a low-Mach, slightly compressible perturbation model about the measured or prescribed steady hydraulic state, not a claim that the complete steady loop pressure distribution is spatially uniform.

### 3.2. Nonlinear perturbation equations

Substituting Eq. (8) into the pressure equation (5), applying the scaling in Eq. (9), and retaining the transient convective contribution gives

$$P_\tau + V_X + MP_X + MVP_X = 0 \tag{11}$$

where subscripts denote partial differentiation. The term $MP_X$ represents advection of a small pressure disturbance by the steady circulation, whereas $MVP_X$ is nonlinear because it contains the product of the velocity and pressure perturbations. The momentum equation is treated in the same way after subtracting the steady hydraulic balance. A dimensionless incremental pump or control forcing is denoted by $S(X,\tau)$. For a turbulent operating point with the Darcy factor frozen at its reference value over a short perturbation, the result is

$$V_\tau + P_X + MV_X + MVV_X + \Gamma(2V + V^2) = S \tag{12}$$

Equation (12) follows from the exact local expansion, valid while the flow direction remains positive,

$$u|u| - U_0^2 = U_0^2[(1+V)^2 - 1] = U_0^2(2V + V^2) \tag{13}$$

Thus, the nonlinear model contains three explicitly identifiable contributions: pressure convection $MVP_X$, momentum convection $MVV_X$, and turbulent quasi-steady friction $\Gamma V^2$. This separation is useful because their magnitudes need not be comparable even when $M$ is small. The dependence of turbulent friction on Reynolds number and roughness is classical; the reference factor will later be evaluated consistently with the selected operating state [13].

### 3.3. Laminar and turbulent friction branches

The frictional nonlinearity requires special care because it disappears in a fully developed laminar pipe flow. Using $f_D = 64/Re$ in Eq. (6), the Darcy resistance reduces exactly to

$$\frac{f_D}{2D}\,u|u| = \frac{32\mu}{\rho D^2}\,u, \qquad (u > 0,\ \text{laminar}) \tag{14}$$

and therefore, its transient increment is linear in $V$. With the present time scale the associated dimensionless damping coefficient is

$$\Lambda_L = \frac{32\mu L}{\rho D^2 c} \tag{15}$$

so that laminar Darcy friction contributes $\Lambda_L\ V$ and no quadratic friction term. By contrast, for a turbulent operating point the frozen-factor approximation of Eq. (12) contains both $2\Gamma V$ and $\Gamma V^2$. If the disturbance causes a sufficiently large Reynolds-number excursion, the full dependence $f_D(Re, \varepsilon/D)$ can be updated instead of frozen; the classical Colebrook relation provides the reference rough-pipe closure [13]. This laminar/turbulent distinction will be retained in the spacecraft applications rather than forcing both fluids into the same friction model.

### 3.4. Consistent linear perturbation model

The linear comparison model must be obtained from Eqs. (11)-(12), not introduced independently. Retaining all first-order perturbation terms and discarding products of perturbations gives

$$P_\tau + V_X + MP_X = 0 \tag{16}$$

and, for the frozen-factor turbulent branch,

$$V_\tau + P_X + MV_X + 2\Gamma V = S \tag{17}$$

For the laminar branch, $2\Gamma V$ in Eq. (17) is replaced by $\Lambda_L\ V$. Equations (16)-(17) therefore retain advection by the steady base flow. This is more consistent than comparing the nonlinear solution with a zero-background wave equation, because the linear and nonlinear models now share the same circulation state, geometry, acoustic scaling, and forcing.

### 3.5. Convected-wave limit and internal consistency check

Define the derivative following the steady circulation as

$$\mathcal{D}_M = \frac{\partial}{\partial\tau} + M\frac{\partial}{\partial X} \tag{18}$$

Then, for homogeneous forcing and a generic linear damping coefficient $\lambda$ (equal to $2\Gamma$ for the frozen turbulent branch or $\Lambda_L$ for the laminar branch), elimination of $V$ from the linear system yields

$$\mathcal{D}_M^2 P - P_{XX} + \lambda\mathcal{D}_M P = 0 \tag{19}$$

In the frictionless limit, the two characteristic wave speeds are

$$C_\pm = M \pm 1 \quad \Leftrightarrow \quad c_\pm = U_0 \pm c \tag{20}$$

which is the expected upstream/downstream acoustic propagation relative to a moving liquid. Finally, taking $M \to 0$ and $\lambda \to 0$ reduces Eq. (19) to

$$P_{\tau\tau} - P_{XX} = 0 \tag{21}$$

the classical dimensionless linear pressure-wave equation. This recovery provides an internal analytical consistency check and agrees with the low-Mach simplifications commonly used in one-dimensional hydraulic-transient theory [10,12].

Equations (11)-(12) and (16)-(17) are the nonlinear and linear pressure-velocity systems carried forward. Their difference is unambiguous: the steady-flow advection terms are common to both models, while the products $MVP_X$, $MVV_X$, and, when applicable, $\Gamma V^2$ constitute the nonlinear corrections. Section 4 defines the numerical scheme, forcing, stability control, and quantitative model-error measures used for verification.

## 4. NUMERICAL METHOD AND QUANTITATIVE VALIDITY METRICS

### 4.1. Closed-loop computational domain and initial state

The nonlinear and linear perturbation systems derived in Section 3 are solved on the dimensionless closed-loop coordinate $0 \le X < 1$. Because the pump is represented as a localized momentum input inside the loop, the regular fluid domain is periodic. Accordingly, pressure and velocity perturbations satisfy

$$P(0,\tau) = P(1,\tau), \qquad V(0,\tau) = V(1,\tau) \tag{22}$$

and the reference transient begins from the steady circulating operating point, so the perturbations are initially zero:

$$P(X,0) = 0, \qquad V(X,0) = 0 \tag{23}$$

The periodic formulation avoids artificial inlet and outlet reflections and is consistent with the physical topology of a recirculating spacecraft loop. Component-level pressure changes are introduced locally rather than by imposing an open-pipe boundary condition.

### 4.2. Finite-time pump disturbance

To remain within the intended quasi-steady wall-friction regime, the baseline excitation is a smooth finite-time change in pump momentum input rather than an instantaneous valve closure. The dimensionless forcing in Eq. (12) is written as

$$S(X,\tau) = A_s\,\chi_p(X)\,h(\tau), \qquad \int_0^1 \chi_p(X)\,\mathrm{d}X = 1 \tag{24}$$

where $A_s$ sets the forcing amplitude and $\chi_{\mathrm{p}}(X)$ is a narrow normalized spatial kernel centered at the pump position. A smooth pulse used for verification and sensitivity calculations is

$$h(\tau)=\begin{cases}\sin^2\left(\frac{\pi\tau}{T_s}\right), & 0\le\tau\le T_s,\\ 0, & \tau>T_s,\end{cases} \tag{25}$$

with $T_s$ the dimensionless disturbance duration. In the spacecraft application stage, the source width is reduced until the predicted peak pressure and the linear-versus-nonlinear difference are insensitive to further localization. This gives a regularized representation of a compact pump element without spreading the forcing throughout the loop.

### 4.3. Spatial discretization and time integration

The dimensionless loop is divided into $N$ equally spaced nodes with $\Delta X = 1/N$. For the smooth-wave regime considered here, first spatial derivatives are evaluated with the fourth-order centered stencil

$$\left.\frac{\partial\phi}{\partial X}\right|_j \approx \frac{-\phi_{j+2}+8\phi_{j+1}-8\phi_{j-1}+\phi_{j-2}}{12\,\Delta X}+\mathcal{O}(\Delta X^4) \tag{26}$$

with periodic index wrapping. Fourth-order finite-difference weights follow the general high-order differentiation framework described by Fornberg [14]. After spatial discretization, the pressure and velocity degrees of freedom are collected into a state vector and advanced by the method of lines:

$$\frac{\mathrm{d}\mathbf{Q}}{\mathrm{d}\tau}=\mathbf{R}(\mathbf{Q},\tau), \qquad \mathbf{Q}=[P_0,\dots,P_{N-1},V_0,\dots,V_{N-1}]^{\mathrm{T}} \tag{27}$$

Time integration uses the classical explicit fourth-order Runge-Kutta method, a standard nonstiff integration scheme [15]:

$$\begin{aligned}\mathbf{k}_1 &= \mathbf{R}(\mathbf{Q}^n,\tau_n)\\ \mathbf{k}_2 &= \mathbf{R}(\mathbf{Q}^n+\Delta\tau/2\,\mathbf{k}_1,\tau_n+\Delta\tau/2)\\ \mathbf{k}_3 &= \mathbf{R}(\mathbf{Q}^n+\Delta\tau/2\,\mathbf{k}_2,\tau_n+\Delta\tau/2)\\ \mathbf{k}_4 &= \mathbf{R}(\mathbf{Q}^n+\Delta\tau\mathbf{k}_3,\tau_n+\Delta\tau)\\ \mathbf{Q}^{n+1} &= \mathbf{Q}^n+\Delta\tau/6\,(\mathbf{k}_1+2\mathbf{k}_2+2\mathbf{k}_3+\mathbf{k}_4)\end{aligned} \tag{28}$$

### 4.4. Time-step control and characteristic-speed check

For the nonlinear principal part, the local dimensionless characteristic +speeds are $C_{\pm}^{loc} = M(1+V)\pm 1$. The time step is therefore selected from the instantaneous maximum propagation speed using

$$C_{\mathrm{CFL}}=\frac{\Delta\tau}{\Delta X}\max_j\{|M(1+V_j)+1|,|M(1+V_j)-1|\} \tag{29}$$

and the production calculations use a conservative target Courant number that is verified by time-step refinement rather than treated as a universal stability constant. Characteristic-speed-based step control is standard for hyperbolic wave systems [16].

The same spatial grid, time step, source history, and initial state are used for each paired linear/nonlinear calculation so that the measured discrepancy is attributable to model physics rather than unequal discretization.

### 4.5. Quantitative linear-versus-nonlinear metrics

Three complementary diagnostics are used. First, the global pressure-field discrepancy over the complete space-time calculation is

$$E_{P,2}=100\,\frac{\left[\sum_n\sum_j\left(P^n_{\mathrm{NL},j}-P^n_{\mathrm{L},j}\right)^2\right]^{1/2}}{\left[\sum_n\sum_j\left(P^n_{\mathrm{NL},j}\right)^2\right]^{1/2}} \tag{30}$$

where subscripts $NL$ and $L$ denote the nonlinear and linear models. Second, the relative difference in the largest positive pressure excursion is

$$E_{P,\max}=100\,\frac{|P_{\max,\mathrm{NL}}-P_{\max,\mathrm{L}}|}{|P_{\max,\mathrm{NL}}|} \tag{31}$$

and, when a distinct pressure maximum can be identified at the observation location, the relative timing difference is

$$E_t=100\,\frac{|\tau_{\max,\mathrm{NL}}-\tau_{\max,\mathrm{L}}|}{\tau_{\max,\mathrm{NL}}} \tag{32}$$

The validity map will be based primarily on the global field metric in Eq. (30) and the peak-pressure metric in Eq. (31). For reporting, differences below 1% will be described as linear-equivalent at the chosen engineering tolerance, differences from 1% to below 5% as a transition regime, and differences of 5% or more as materially nonlinear. These are explicit operational bands for this study, not universal fluid-mechanical thresholds; their sensitivity will be discussed with the final results.

### 4.6. Verification and grid-convergence protocol

Numerical verification is performed before any spacecraft parameter interpretation. Nested grids are used so that solutions can be compared at coincident nodes. The observed spatial convergence order is evaluated as

$$r_{\mathrm{obs}}=\log_2\left(\frac{\|Q_N-RQ_{2N}\|_2}{\|RQ_{2N}-R^2Q_{4N}\|_2}\right) \tag{33}$$

where $\mathcal{R}$ restricts a fine-grid solution to the coincident nodes of the next coarser grid. For smooth solutions, fourth-order spatial behavior is expected until temporal or round-off error dominates. In addition to grid refinement, the solver is subjected to the analytical low-nonlinearity limit established in Section 3 and to a smooth characteristic-wave benchmark before application results are accepted.

**Table 2**. Numerical verification protocol used before spacecraft application calculations.

| **Check** | **Procedure** | **Acceptance criterion / purpose** |
|---|---|---|
| Spatial refinement | Repeat on nested N, 2N, and 4N grids | Observed order approaches the designed fourth-order behavior for a smooth benchmark. |
| Time-step refinement | Reduce Δτ at fixed fine grid | Pressure metrics and wave timing become insensitive to further reduction. |
| Linear-limit recovery | Reduce disturbance/nonlinear terms while retaining the same base flow | Nonlinear solution approaches the consistent moving-base linear solution. |
| Smooth-wave benchmark | Compare with a characteristic solution before steepening | Separates numerical error from model-form differences. |
| Pump localization | Reduce the width of the pump-source kernel while preserving its integral | Peak pressure and linear/nonlinear metrics become insensitive to source width. |
| Friction branch | Check laminar and turbulent closures separately | Prevents attributing quadratic-friction effects to convective nonlinearity. |

Only after the checks in Table 2 are satisfied are spacecraft-specific parameters introduced. This separation is deliberate: it ensures that a later linear-versus-nonlinear difference is interpreted as a physical model-form effect rather than a numerical artifact. The quantitative convergence and benchmark results are reported in Section 5 before the spacecraft-informed applications are evaluated.

## 5. NUMERICAL VERIFICATION AND CONVERGENCE RESULTS

### 5.1. Smooth nonlinear characteristic benchmark

The numerical solver is first tested independently of any spacecraft parameter interpretation. Setting the source and friction terms to zero and choosing the smooth simple-wave state $P = V = q$ reduces Eqs. (11)-(12) to the scalar quasilinear equation

$$q_\tau + [1 + M(1 + q)]q_X = 0 \tag{34}$$

For the periodic initial condition $q_0(X) = A_q\, sin(2\pi X)$, the pre-steepening characteristic solution is given implicitly by

$$q(X,\tau) = q_0(\xi) = A_q \sin(2\pi\xi)$$

$$X = \xi + \left[1 + M\left(1 + q_0(\xi)\right)\right]\tau \tag{35}$$

Characteristic crossing first occurs when the mapping from $\xi$ to $X$ loses monotonicity, which for this sinusoidal initial state gives

$$\tau_s = \frac{1}{2\pi M A_q} \tag{36}$$

The verification case uses $A_q = 0.20$, $M = 0.20$, and $\tau_f = 0.25$. Hence $\tau_s \approx 3.98$, so the calculation remains well inside the smooth regime and does not test a shock-capturing problem.

The implicit characteristic coordinate in Eq. (35) is solved to a Newton-iteration tolerance of $10^{-14}$ and used as the reference solution.

### 5.2. Spatial and temporal convergence

For each grid, the relative pressure error at the final time is evaluated as

$$e_N = \frac{\|P_N(\tau_f) - P_{\text{exact}}(\tau_f)\|_2}{\|P_{\text{exact}}(\tau_f)\|_2} \tag{37}$$

Table 3 shows a nearly ideal fourth-order reduction of the error under successive grid doubling, consistent with the centered fourth-order stencil and RK4 integration used in Section 4 [14,15]. The error falls from $2.81\times10^{-4}$ on 25 nodes to $2.72\times10^{-10}$ on 800 nodes, while the observed order approaches 4.000.

**Table 3**. Grid-convergence results for the smooth nonlinear characteristic benchmark.

| **Grid nodes N** | **Relative error $e_N$** | **Observed order** |
|---|---|---|
| 25 | $2.8131 \times 10^{-4}$ | — |
| 50 | $1.7751 \times 10^{-5}$ | 3.9862 |
| 100 | $1.1121 \times 10^{-6}$ | 3.9965 |
| 200 | $6.9548 \times 10^{-8}$ | 3.9991 |
| 400 | $4.3474 \times 10^{-9}$ | 3.9998 |
| 800 | $2.7172 \times 10^{-10}$ | 3.9999 |

A separate time-step refinement is performed on the intentionally coarse $N = 50$ grid so that temporal effects remain observable. Table 4 shows that reducing the target Courant number from 0.2 to 0.1 changes the final relative error by only about 0.032%, demonstrating that the spatial discretization, rather than the time step, controls the reported production-grid error at the adopted setting. A target $C_{\text{CFL}} = 0.2$ is therefore retained for subsequent paired calculations.

**Table 4**. Time-step refinement for the nonlinear benchmark at $N = 50$.

| Target $C_{CFL}$ | Time steps | Relative error $e_N$ |
|---|---|---|
| 1.2 | 13 | $2.5701 \times 10^{-5}$ |
| 0.8 | 20 | $1.9119 \times 10^{-5}$ |
| 0.4 | 39 | $1.7845 \times 10^{-5}$ |
| 0.2 | 78 | $1.7755 \times 10^{-5}$ |
| 0.1 | 155 | $1.7749 \times 10^{-5}$ |

### 5.3. Recovery of the linear limit and friction-branch check

The second verification asks whether the nonlinear implementation approaches the consistent moving-base linear model as the nonlinear coefficient becomes small.

With $A_q = 0.20$, $\Gamma = 0$, and otherwise identical initial data and numerics, the global discrepancy defined in Eq. (30) decreases almost exactly in proportion to $M$ (Table 5). At $M = 10^{-3}$, the nonlinear/linear field discrepancy has fallen to 0.00908%. This establishes the required numerical recovery of the analytical low-nonlinearity limit.

**Table 5**. Numerical recovery of the moving-base linear limit.

| M | Global pressure discrepancy $E_{P,2}$ (%) |
|---|---|
| 0.100 | 0.90810 |
| 0.050 | 0.45409 |
| 0.020 | 0.18165 |
| 0.010 | 0.09082 |
| 0.005 | 0.04541 |
| 0.001 | 0.00908 |

The nonlinear turbulent-friction branch was also checked by self-convergence because no closed-form damped solution is required for this purpose.

For $M = 0.05$, $\Gamma = 0.05$, $A_q = 0.20$, and $\tau_f = 0.25$, nested-grid comparisons gave observed orders of 3.9978, 3.9994, and 3.9999 for the 50/100/200, 100/200/400, and 200/400/800 grid triplets, respectively. Thus, introducing the quadratic friction term does not degrade the designed smooth-solution convergence rate.

### 5.4. Numerical verification decision

The three required numerical gates are therefore satisfied:

(i) the nonlinear solver reproduces an independent smooth characteristic solution with fourth-order convergence;

(ii) time-step refinement demonstrates that the adopted Courant setting does not control the reported grid error; and

(iii) the nonlinear solution approaches the moving-base linear solution continuously as the nonlinear coefficient is reduced. The turbulent-friction branch independently retains the expected convergence behavior.

Consequently, the numerical method is considered verified for the smooth single-phase transient regime addressed by this study. These tests establish numerical reliability only; they do not by themselves establish the magnitude of nonlinear effects in a real spacecraft loop. That physical question is addressed next using traceable spacecraft-informed fluid properties, geometry ranges, and operating conditions.

## 6. SPACECRAFT-INFORMED APPLICATION I: HFE-7200 THERMAL-CONTROL LOOP

### 6.1. Application definition and traceability

The first application is anchored to the European Service Module (ESM) active thermal-control architecture. Published ESM design documentation describes a single-phase fluid-loop architecture using an HFE-7200-series coolant to collect spacecraft thermal loads and reject heat through the radiator system [17]. The calculation below is therefore spacecraft-informed, but it is not presented as a reconstruction of the proprietary flight hydraulic network. Public literature establishes the fluid and architecture, whereas the complete flight-loop length, tube diameters, local loss coefficients, compliance distribution, and absolute hydraulic operating pressures are not all publicly specified. HFE-7200 has a high liquid density and low viscosity; dedicated thermophysical-property measurements report density and kinematic viscosity over broad temperature ranges [18].

Independent acoustic measurements on ethyl nonafluorobutyl ether, the principal HFE-7200 constituent family, establish the availability of liquid sound-speed data over relevant temperatures and pressures [19]. Because the effective pressure-wave celerity of a flight loop also depends on tube-wall compliance and component flexibility, the present case uses a representative effective value rather than labeling the chosen celerity as a measured Orion parameter.

### 6.2. Representative operating point

Table 6 defines the baseline calculation. Fluid properties are representative of HFE-7200 near room temperature, while the loop length, hydraulic diameter, mean speed, and effective celerity are deliberately labeled modeling parameters. The chosen geometry produces a turbulent reference state, allowing both convective and quadratic-friction nonlinearities in Eq. (12) to remain active. For the baseline state, the Reynolds number is

$$\mathrm{Re}_0 = \frac{\rho U_0 D}{\mu} = 2.34 \times 10^4 \tag{38}$$

and the hydraulically smooth Colebrook relation gives a reference Darcy factor of approximately $f_0 = 0.0249$. The resulting dimensionless parameters are

$$M = 1.67 \times 10^{-3}, \quad \Gamma = 2.08 \times 10^{-2}, \; \varepsilon_b = \Gamma M = 3.46 \times 10^{-5} \tag{39}$$

so, the neglected steady-gradient convection scale in Eq. (10) is extremely small. The pressure and time scales used to convert the dimensionless solution are

$$p_c = \rho c U_0 = 8.58 \times 10^5 \text{ Pa}, \quad t_c = \frac{L}{c} = 1.67 \times 10^{-2} \text{ s} \tag{40}$$

**Table 6**. Representative HFE-7200 spacecraft-loop parameters used for the first application.

| **Quantity** | **Baseline value** | **Basis / interpretation** |
|---|---|---|
| Coolant | HFE-7200 | Spacecraft fluid identified in ESM design literature [17] |
| Reference temperature, T | 298 K | Representative property state |
| Density, ρ | 1430 kg $m^{-3}$ | Consistent with published HFE-7200 property data [18] |
| Dynamic viscosity, μ | 0.61 mPa s | Representative near-room-temperature value; consistent with published property measurements [18] |
| Equivalent loop length, L | 10 m | Representative modeling parameter; not a disclosed Orion dimension |
| Hydraulic diameter, D | 10 mm | Representative modeling parameter |
| Steady speed, $U_0$ | 1.0 m $s^{-1}$ | Representative circulating speed |
| Effective wave celerity, c | 600 m $s^{-1}$ | Representative compliant-loop value; sensitivity parameter, not asserted flight data |
| Dimensionless disturbance duration, $T_s$ | 3 | Three acoustic characteristic times |
| Physical disturbance duration, $t_s$ | 0.050 s | $t_s = T_s$ t_c |
| Production grid | N = 200, C_CFL = 0.2 | Within the verified fourth-order regime of Section 5 |

### 6.3. Linear-versus-nonlinear transient response

The source amplitude is first set to $A_s$ = 0.20 and applied for $T_s$ = 3. This produces a maximum velocity perturbation of $0.287U_0$, large enough to test the nonlinear terms without flow reversal. Over six acoustic travel times (0.10 s), the maximum nonlinear pressure excursion anywhere in the loop is $P_{\max}$ = 0.08714, corresponding to approximately 74.8 kPa with Eq. (40). Despite this finite disturbance, the paired solutions remain very close: the global pressure-field discrepancy defined by Eq. (30) is $E_{P,2}$ = 0.0667%, while the peak-pressure metric of Eq. (31) is only 0.0059%. Figure 1 shows the pressure history at $X$ = 0.5. The near-complete overlap is itself the relevant result: at this operating point, retaining the nonlinear corrections changes the transient prediction by far less than one percent.

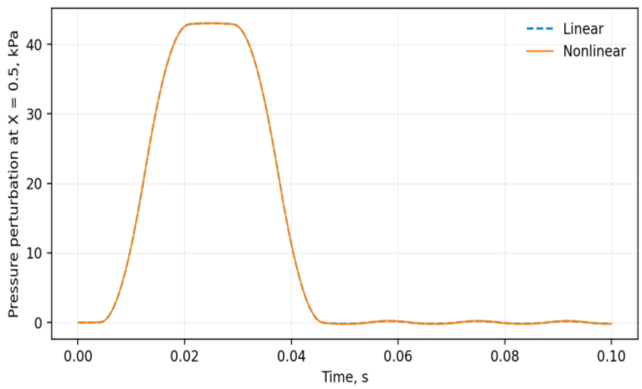


**Figure 1**. Linear and nonlinear pressure perturbations at $X$ = 0.5 for the representative HFE-7200 loop ($A_s$ = 0.20).

### 6.4. Disturbance-amplitude sensitivity

To test whether the conclusion depends on an exceptionally weak perturbation, the same loop is recalculated over a broad forcing range. Table 7 reports the maximum velocity perturbation, maximum nonlinear pressure excursion, and the two linear-versus-nonlinear error measures. Even when the peak velocity perturbation exceeds 60% of the steady speed, the global pressure discrepancy remains below 0.15% for this parameter set.

**Table 7.** Disturbance-amplitude sensitivity for the representative HFE-7200 loop.

| $A_s$ | max \|V\| | max \|V\| (%) | max $\Delta p_{NL}$ (kPa) | $E_{P,2}$ (%) | $E_{P,max}$ (%) |
|---|---|---|---|---|---|
| 0.05 | 0.0719 | 7.2 | 18.7 | 0.0168 | 0.0015 |
| 0.10 | 0.1436 | 14.4 | 37.4 | 0.0336 | 0.0030 |
| 0.20 | 0.2867 | 28.7 | 74.8 | 0.0667 | 0.0059 |
| 0.30 | 0.4292 | 42.9 | 112.1 | 0.0995 | 0.0089 |
| 0.45 | 0.6418 | 64.2 | 168.2 | 0.1481 | 0.0133 |

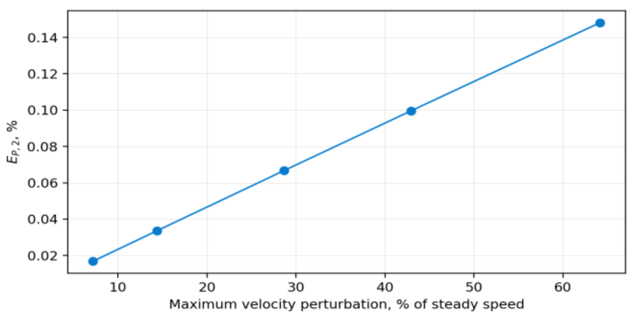


**Figure 2**. Growth of the global linear-versus-nonlinear pressure discrepancy with disturbance amplitude for the representative HFE-7200 loop.

### 6.5. Application-I interpretation and limitations

The first spacecraft-informed case therefore gives a clear result: the nonlinear terms are physically present, but they are not numerically important for the representative low-Mach HFE-7200 operating point considered here.

The dominant reason is $M \approx 1.7\times10^{-3}$; convective nonlinearities are consequently weak, and the quadratic-friction correction remains modest over the smooth finite-time disturbance. For this case, the moving-base linear model is not merely computationally convenient, it is quantitatively justified to substantially better than a 1% pressure-field criterion. This conclusion is intentionally restricted to the tested parameter set. The exact flight-loop geometry, compliance, component losses, base pressure, and detailed pump transient are not fully available in the public sources used here. Therefore, the calculation should be interpreted as an Orion/ESM-informed engineering case rather than flight-model validation. Absolute cavitation margin is likewise not asserted without the proprietary base-pressure distribution; instead, the present result establishes the magnitude of the transient pressure perturbation that such a check would need to accommodate.

## 7. SPACECRAFT-INFORMED APPLICATION II AND COMPARATIVE VALIDITY MAP

### 7.1. PGW internal-loop basis

The second application represents the internal propylene-glycol/water (PGW) cooling loop used in Orion-class human-spaceflight thermal-control architectures. Dynamic Orion ATCS modeling has treated the internal and external loops as coupled pumped-fluid networks [20].

The present calculation does not reproduce the proprietary Orion hydraulic network; instead, it uses a representative 50/50 PGW mixture and an Orion-informed tube scale so that the governing model can be tested in a physically distinct, high-viscosity regime. Experimental studies provide density and viscosity data for aqueous propylene-glycol mixtures over temperatures relevant to thermal-control service [21], while ultrasonic measurements confirm composition-dependent acoustic behavior in the water + propylene-glycol system [22]. As in Section 6, the effective loop wave celerity is treated as a modeling parameter because the flight value depends on distributed tubing and component compliance in addition to the liquid bulk modulus.

### 7.2. Representative PGW operating point

**Table 8**. Representative PGW spacecraft-loop parameters used for the second application

| Quantity | Baseline value | Basis / interpretation |
|---|---|---|
| Coolant | 50/50 PGW | Representative internal-loop mixture |
| Reference temperature, T | 298 K | Representative property state |
| Density, ρ | 1040 kg m$^{-3}$ | Consistent with aqueous-PG property measurements [21] |
| Dynamic viscosity, μ | 6.0 mPa s | Representative 50/50-mixture value near room temperature [21] |
| Equivalent loop length, L | 10 m | Representative modeling parameter |
| Hydraulic diameter, D | 10.9 mm | Representative Orion-informed tube scale |
| Steady speed, $U_0$ | 0.30 m s$^{-1}$ | Representative mean circulation speed |
| Effective wave celerity, c | 500 m s$^{-1}$ | Representative compliant-loop value |
| Dimensionless disturbance duration, $T_s$ | 3 | Three acoustic characteristic times |
| Physical disturbance duration, $t_s$ | 0.060 s | $t_s = T_s$ t_c |
| Production grid | N = 240, C_CFL = 0.2 | Within verified numerical regime |

The baseline Reynolds number is

$$\mathrm{Re}_0 = \frac{\rho U_0 D}{\mu} = 5.67\times10^{2} \qquad (41)$$

which is firmly laminar. Substituting $f_D = 64/\mathrm{Re}$ into the Darcy term reduces the distributed wall resistance to a linear viscous contribution after subtraction of the steady pressure gradient. The resulting dimensionless laminar damping coefficient is

$$\Lambda_L = \frac{32\mu L}{\rho D^2 c} = 3.11\times10^{-2} \qquad (42)$$

while the base acoustic Mach number and the dimensional scales are

$$M = 6.00\times10^{-4} \qquad p_c = \rho c U_0 = 1.56\times10^{5}\ \mathrm{Pa}$$
$$t_c = \frac{L}{c} = 2.00\times10^{-2}\ \mathrm{s} \qquad (43)$$

For this laminar case, quadratic friction does not supply an additional nonlinearity. Consequently, the difference between the full and linearized systems is generated almost entirely by the convective Navier-Stokes terms proportional to $M$.

### 7.3. PGW linear-versus-nonlinear response

With $A_s = 0.20$, the maximum velocity perturbation is $0.291U_0$ and the maximum nonlinear pressure perturbation is $P_{\max} = 0.08710$, corresponding to approximately 13.6 kPa. The global discrepancy is only $E_{P,2} = 0.0116\%$, and the peak-pressure difference is 0.0023%. Figure 3 shows the pressure history at $X = 0.5$; the curves are visually indistinguishable at ordinary plotting resolution.

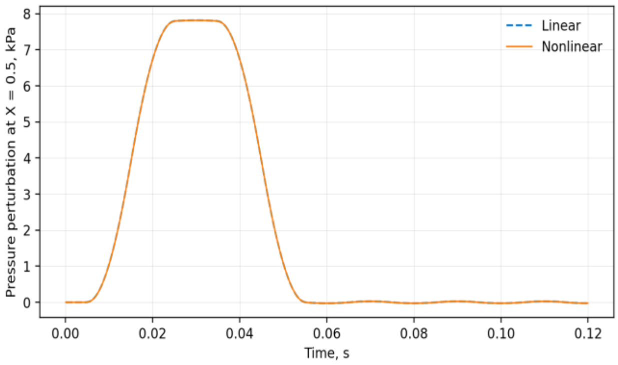


**Figure 3**. Linear and nonlinear pressure perturbations at $X$ = 0.5 for the representative PGW loop ($A_s$ = 0.20).

**Table 9**. Disturbance-amplitude sensitivity for the representative laminar PGW loop.

| $A_s$ | max \|V\| | max \|V\| (%) | max $\Delta p_{NL}$ (kPa) | $E_{P,2}$ (%) | $E_{P,max}$ (%) |
|---|---|---|---|---|---|
| 0.05 | 0.0727 | 7.3 | 3.40 | 0.0029 | 0.0006 |
| 0.10 | 0.1454 | 14.5 | 6.79 | 0.0058 | 0.0012 |
| 0.20 | 0.2908 | 29.1 | 13.59 | 0.0116 | 0.0023 |
| 0.30 | 0.4362 | 43.6 | 20.38 | 0.0173 | 0.0035 |
| 0.45 | 0.6543 | 65.4 | 30.57 | 0.0260 | 0.0052 |

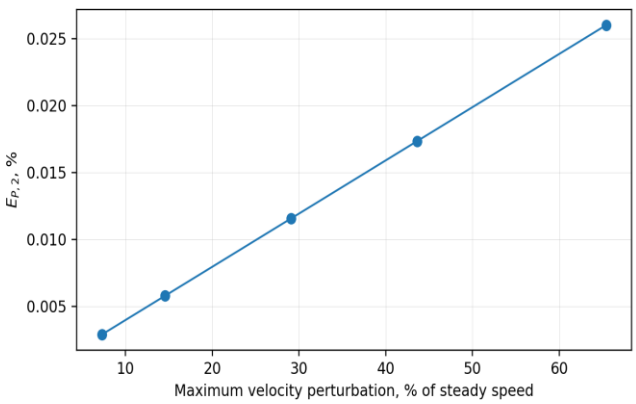


**Figure 4**. Linear-versus-nonlinear pressure discrepancy for the representative laminar PGW loop.

### 7.4. Comparison of the two spacecraft-informed loops

The two applications occupy different hydraulic regimes. The HFE-7200 case is turbulent and therefore contains both convective and quadratic-friction nonlinearities, whereas the PGW case is laminar and retains only the convective nonlinear correction after the steady state is removed. Figure 5 compares the global pressure discrepancy against disturbance strength. Across the common range, the HFE-7200 case consistently exhibits the larger nonlinear correction, but both remain far below 1% for the representative low-Mach spacecraft conditions.

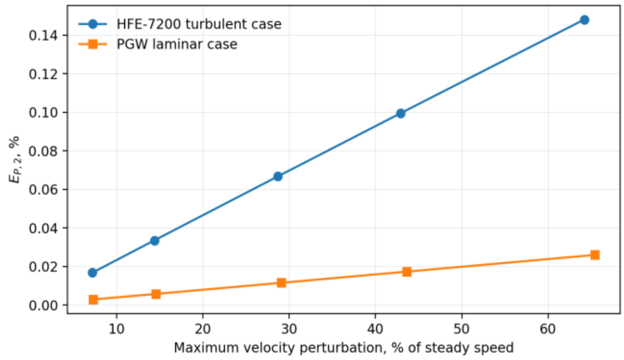


**Figure 5**. Comparison of the global linear-versus-nonlinear pressure discrepancy for the representative HFE-7200 and PGW spacecraft loops.

### 7.5. Dimensionless validity map

To separate the spacecraft-specific conclusion from the more general behavior of the reduced model, a dimensionless parametric sweep was performed for a turbulent reference family with $\Gamma = 0.02$. The base acoustic Mach number was varied from $5\times10^{-4}$ to 0.10 and the forcing amplitude from 0.05 to 0.80. This sweep deliberately extends well beyond the two spacecraft baselines and is used only to identify the transition between linear and nonlinear response regimes.

$$\mathcal{R} = \begin{cases} \text{linear-dominant}, & E_{P,2} < 1\%, \\ \text{weakly nonlinear}, & 1\% \le E_{P,2} < 5\%, \\ \text{nonlinear-sensitive}, & E_{P,2} \ge 5\%. \end{cases} \tag{44}$$

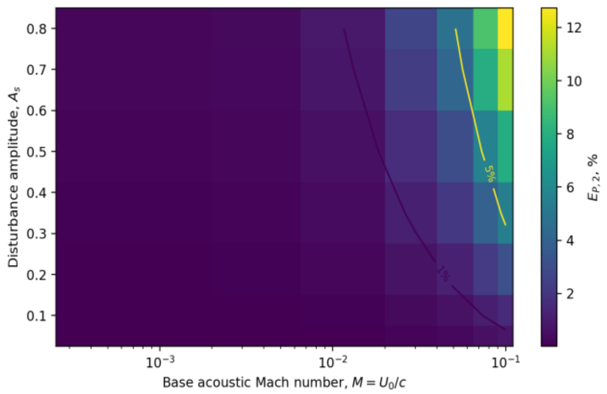


**Figure 6**. Dimensionless model-validity map for a turbulent reference family ($\Gamma$ = 0.02). Contours indicate the operational 1% and 5% pressure-discrepancy thresholds.

The thresholds in Eq. (44) are operational engineering criteria adopted for model-selection purposes; they are not universal physical constants. Figure 6 shows that the spacecraft-relevant low-Mach region lies well inside the linear-dominant domain, whereas errors above 1% emerge when $M$ and disturbance amplitude become simultaneously larger. In the tested family, the 5% contour appears only at substantially higher Mach number and strong forcing, approximately $M \gtrsim 0.08$ for $A_s$ around 0.5 and above. The combined result answers the central research question for the two-baseline spacecraft-informed applications: nonlinear terms are present in the governing equations, but the consistent moving-base linear model is sufficient to much better than the 1% criterion under the representative HFE-7200 and PGW conditions. The nonlinear formulation remains valuable because it establishes the error of the linearization and identifies the parameter direction in which that approximation eventually fails.

## 8. RESULTS AND DISCUSSION

### 8.1. Numerical credibility and model hierarchy

The numerical verification establishes that the differences reported between the linear and nonlinear models are not artifacts of spatial or temporal discretization. The smooth nonlinear benchmark converges at essentially fourth order, consistent with the selected finite-difference and Runge-Kutta formulations [14,15]. The independently tested turbulent-friction branch exhibits the same asymptotic convergence behavior, and the nonlinear system approaches the moving-base linear formulation continuously as M decreases.

This distinction is important: numerical convergence does not prove that a reduced physical model is complete, but it does show that the model-form discrepancies discussed below are resolved well above the verified numerical error floor.

The hierarchy produced by the derivation is also physically transparent. Convective corrections scale with the base acoustic Mach number $M$, whereas turbulent quasi-steady resistance adds a second nonlinearity through the velocity-squared friction law. In the laminar PGW case, substituting $f$ = 64/Re removes that quadratic contribution after the steady gradient is subtracted, leaving convection as the principal nonlinear correction.

This separation is consistent with the broader hydraulic-transient literature, which distinguishes convective effects from frictional and unsteady-wall-shear mechanisms [6,8,9,10,12].

### 8.2. Spacecraft-informed application results

The two spacecraft-informed calculations deliberately occupy different hydraulic regimes. The HFE-7200 reference loop has $Re_0 \approx 2.34\times10^4$ and $M \approx 1.67\times10^{-3}$, so both convective and quadratic-friction nonlinearities are active. The 50/50 PGW case has $Re_0 \approx 5.67\times10^2$ and $M = 6.00\times10^{-4}$, so the steady state is laminar and the transient comparison isolates the much weaker convective correction. Table 10 summarizes the principal results at the common disturbance level $A_s$ = 0.20.

**Table 10**. Summary of the two spacecraft-informed applications at $A_s$ = 0.20.

| Case | Re₀ | M | Friction regime | max $\Delta p_{NL}$ (kPa) | $E_{P,2}$ (%) | $E_{P,max}$ (%) |
|---|---|---|---|---|---|---|
| **HFE-7200** | $2.34\times10^4$ | $1.67\times10^{-3}$ | Turbulent | 74.8 | 0.0667 | 0.0059 |
| **50/50 PGW** | $5.67\times10^2$ | $6.00\times10^{-4}$ | Laminar | 13.6 | 0.0116 | 0.0023 |

For HFE-7200, the global pressure discrepancy at $A_s$ = 0.20 is 0.0667%, rising monotonically to only 0.1481% at $A_s$ = 0.45. The PGW discrepancy is still smaller, increasing from 0.0116% at $A_s$ = 0.20 to 0.0260% at $A_s$ = 0.45.

These values are far below the operational 1% boundary adopted in Eq. (44). The result therefore does not support a claim that a nonlinear model is required for the representative low-Mach spacecraft conditions considered here. Instead, it quantitatively validates the simpler moving-base linear model within the tested envelope.

This conclusion is consistent with the broader spacecraft context. Single-phase mechanically pumped loops have long been modeled dynamically for spacecraft thermal-control applications [3,20], and recent high-fidelity space-station work continues to use conservation-law-based fluid-loop models for prediction and health monitoring [5].

Flight experience also demonstrates that pressure variation is an operationally relevant quantity: the Chang'e-5 pumped-fluid-loop thermal bus reported an on-orbit pressure-variation history during system reconfiguration that was consistent with ground tests [23].

The present study complements these system-level efforts by quantifying the hydraulic model complexity required for a specified transient regime.

### 8.3. Interpretation of the validity map

The dimensionless sweep extends the conclusion beyond the two baseline applications. Within the turbulent reference family $\Gamma$= 0.02, the spacecraft-relevant low-Mach region remains linear-dominant over the investigated forcing amplitudes. Errors above 1% appear only when $M$ and disturbance strength increase together, and the 5% contour is reached only at substantially higher Mach number and strong forcing, approximately $M \gtrsim 0.08$ for $A_s$ near 0.5 and above. Thus, disturbance amplitude cannot be used as the sole criterion for model selection; a large velocity perturbation may still produce a small linearization error when the acoustic Mach number is very low.

The map should therefore be interpreted as a model-selection aid rather than as a universal boundary. Its numerical contours depend on Γ, the source shape and duration, the assumed wall compliance, and the selected error norm.

The more general physical conclusion is robust: the nonlinear correction grows through the combined action of convective scaling, friction regime, and disturbance strength. A spacecraft engineer can consequently use the nonlinear formulation as a verification model and retain the linear model for repeated design calculations once the operating point has been shown to lie within an acceptable error band.

### 8.4. Contribution relative to previous work

The underlying one-dimensional nonlinear pressure-velocity equations are not new, and the present work does not claim otherwise. Modern hydraulic-transient studies already retain convective terms, detailed friction models, and fluid-structure interaction when required [6,7,8,9,10,11,12].

Likewise, spacecraft MPFL literature includes transient system simulation, thermal-control design, component modeling, and high-fidelity operational-loop prediction [3,4,5,20,23].

The contribution of the present study is the bridge between these two bodies of work: the same Navier-Stokes-derived conservation-law system is used to construct a paired moving-base linear and nonlinear model, the numerical pair is independently verified, the two principal sources of nonlinearity are separated by flow regime, and an explicit pressure-error validity map is then applied to two spacecraft-informed single-phase loops.

A targeted literature audit performed for the final manuscript did not identify a prior publication whose stated objective and methodology match this combined linear-versus-nonlinear validity framework for single-phase spacecraft pumped-fluid loops. This statement is intentionally narrower than a universal "first-ever" claim; it defines the defensible novelty as the quantitative model-selection framework and its spacecraft-specific interpretation, rather than the governing equations or the existence of spacecraft pressure transients themselves.

### 8.5. Limitations and future work

The results must be interpreted within the reduced-order assumptions. The two applications are spacecraft-informed representative loops, not reconstructions of proprietary flight hydraulic networks. Equivalent length, effective wave celerity, base pressure, distributed compliance, minor losses, and pump transfer characteristics would require mission-specific data for flight-model validation. The baseline solver also assumes constant fluid properties, single-phase operation, one-dimensional flow, and quasi-steady wall friction. Rapid transients may require an unsteady-friction closure [8,9], while stronger fluid-structure coupling may require explicit pipe-wall dynamics [11].

Future work should therefore combine measured loop geometry and pressure histories with uncertainty propagation in c, f, component losses, and fluid properties; incorporate frequency-dependent wall friction and local component models; and couple the hydraulic model to an energy equation when pressure-wave and thermal time scales overlap. Experimental or flight-data comparison would provide the next level of physical validation beyond the numerical verification performed here.

## 9. CONCLUSIONS

**1.** A Navier-Stokes-based one-dimensional pressure-velocity system was derived for a slightly compressible liquid circulating about a nonzero steady base flow. Convective inertia and flow-regime-dependent wall friction were retained in the nonlinear model, and a mathematically consistent linear perturbation model was obtained from the same equations.

**2.** The fourth-order finite-difference/RK4 implementation was independently verified. The smooth nonlinear benchmark showed essentially fourth-order convergence and a relative error of $2.72\times10^{-10}$ at $N$ = 800, while the nonlinear solution recovered the moving-base linear limit as M tended to zero.

**3.** For the representative turbulent HFE-7200 loop, the global pressure discrepancy was 0.0667% at $A_s$ = 0.20 and remained below 0.15% even at $A_s$ = 0.45. For the representative laminar 50/50 PGW loop, the corresponding values were 0.0116% and 0.0260%.

**4.** The spacecraft-informed cases therefore support use of the consistent linear model for the tested low-Mach operating conditions. The nonlinear model is nevertheless essential as a verification model because it quantifies the error introduced by linearization rather than assuming that error to be negligible.

**5.** The dimensionless validity map shows that nonlinear sensitivity increases jointly with acoustic Mach number, disturbance amplitude, and frictional nonlinearity. In the tested turbulent reference family, the 5% discrepancy level occurs only at substantially higher Mach number and strong forcing, near M $\gtrsim$ 0.08 for $A_s$ around 0.5 and above.

**6.** The principal contribution is consequently a quantitative model-validity framework for selecting between linear and nonlinear transient descriptions in single-phase spacecraft pumped-fluid loops. Mission-specific geometry, compliance, component dynamics, and measured pressure data are the logical next steps for flight-system validation.

## REFERENCES

[1] Y.-G. Lv, Y.-T. Wang, T. Meng, Q.-W. Wang, and W.-X. Chu, "Review on thermal management technologies for electronics in spacecraft environment," Energy Storage and Saving, vol. 3, no. 3, pp. 153-189, 2024. https://doi.org/10.1016/j.enss.2024.03.001 Google Scholar

[2] R. C. Consolo Jr. and S. K. S. Boetcher, "Advances in spacecraft thermal control," Advances in Heat Transfer, vol. 56, pp. 1-50, 2023. https://doi.org/10.1016/bs.aiht.2023.04.001 Google Scholar

[3] E. Kotlyarov, R. Reuvers, P. van Put, T. Tjiptahardja, A. S. Galouye-Merino, P. Hugonnot, and B. Daly, "Modeling and correlation of an actively-controlled single phase mechanically-pumped fluid loop," SAE Technical Paper

2007-01-3122, 2007. https://doi.org/10.4271/2007-01-3122 Google Scholar

[4] J.-X. Wang, Y.-Z. Li, H.-S. Zhang, S.-N. Wang, Y.-H. Liang, W. Guo, Y. Liu, and S.-P. Tian, "A highly self-adaptive cold plate for the single-phase mechanically pumped fluid loop for spacecraft thermal management," Energy Conversion and Management, vol. 111, pp. 57-66, 2016. https://doi.org/10.1016/j.enconman.2015.12.051 Google Scholar

[5] C. Liu, L. Chen, J. Ding, L. Huang, and D. Shangguan, "Model-data hybrid thermal management and health monitoring of the space station application fluid loop," Results in Engineering, vol. 29, Art. no. 109387, 2026. https://doi.org/10.1016/j.rineng.2026.109387 Google Scholar

[6] M. R. A. Kumar, J. H. Pu, P. R. Hanmaiahgari, and M. F. Lambert, "Insights into CFD modelling of water hammer," Water, vol. 15, no. 22, Art. no. 3988, 2023. https://doi.org/10.3390/w15223988 Google Scholar

[7] A. E. Vardy, "On sources of damping in water-hammer," Water, vol. 15, no. 3, Art. no. 385, 2023. https://doi.org/10.3390/w15030385 Google Scholar

[8] O. M. Abdeldayem, D. Ferras, S. van der Zwan, and M. Kennedy, "Analysis of unsteady friction models used in engineering software for water hammer analysis: Implementation case in WANDA," Water, vol. 13, no. 4, Art. no. 495, 2021. https://doi.org/10.3390/w13040495 Google Scholar

[9] A. Bergant, A. R. Simpson, and J. Vitkovsky, "Developments in unsteady pipe flow friction modelling," Journal of Hydraulic Research, vol. 39, no. 3, pp. 249-257, 2001. https://doi.org/10.1080/00221680109499828 Google Scholar

[10] F. Plouraboué, "Review on water-hammer waves mechanical and theoretical foundations," European Journal of Mechanics - B/Fluids, vol. 108, pp. 237-271, 2024. https://doi.org/10.1016/j.euromechflu.2024.08.001 Google Scholar

[11] D. Ferras, P. A. Manso, A. J. Schleiss, and D. I. C. Covas, "One-dimensional fluid-structure interaction models in pressurized fluid-filled pipes: A review," Applied Sciences, vol. 8, no. 10, Art. no. 1844, 2018. https://doi.org/10.3390/app8101844 Google Scholar

[12] Y. Cai, J. Wei, Q. Hou, H. Fan, and A. S. Tijsseling, "A Lagrangian particle model for one-dimensional transient pipe flow with moving boundary," Engineering Applications of Computational Fluid Mechanics, vol. 19, no. 1, Art. no. 2452360, 2025. https://doi.org/10.1080/19942060.2025.2452360 Google Scholar

[13] C. F. Colebrook, "Turbulent flow in pipes, with particular reference to the transition region between the smooth and rough pipe laws," Journal of the Institution of Civil Engineers, vol. 11, no. 4, pp. 133-156, 1939. https://doi.org/10.1680/ijoti.1939.13150 Google Scholar

[14] B. Fornberg, "Generation of finite difference formulas on arbitrarily spaced grids," Mathematics of Computation, vol. 51, no. 184, pp. 699-706, 1988. https://doi.org/10.1090/S0025-5718-1988-0935077-0 Google Scholar

[15] E. Hairer, S. P. Nørsett, and G. Wanner, Solving Ordinary Differential Equations I: Nonstiff Problems, 2nd ed. Berlin, Heidelberg: Springer, 1993. https://doi.org/10.1007/978-3-540-78862-1 Google Scholar

[16] R. J. LeVeque, Finite Volume Methods for Hyperbolic Problems. Cambridge: Cambridge University Press, 2002. https://doi.org/10.1017/CBO9780511791253 Google Scholar

[17] P. Berthe, K. Schubert, J. A. Grantier, K. Pietsch, P. Angelillo, and L. Price, "The Multi-purpose Crew Vehicle European Service Module: a European contribution to human exploration," in AIAA SPACE 2013 Conference and Exposition, AIAA 2013-5477, 2013. https://doi.org/10.2514/6.2013-5477 Google Scholar

[18] M. H. Rausch, L. Kretschmer, S. Will, A. Leipertz, and A. P. Fröba, "Density, surface tension, and kinematic viscosity of hydrofluoroethers HFE-7000, HFE-7100, HFE-7200, HFE-7300, and HFE-7500," Journal of Chemical & Engineering Data, vol. 60, no. 12, pp. 3759-3765, 2015. https://doi.org/10.1021/acs.jced.5b00691 Google Scholar

[19] M. M. Piñeiro, F. Plantier, D. Bessières, J. L. Legido, and J. L. Daridon, "High-pressure speed of sound measurements in methyl nonafluorobutyl ether and ethyl nonafluorobutyl ether," Fluid Phase Equilibria, vols. 222-223, pp. 297-302, 2004. https://doi.org/10.1016/j.fluid.2004.06.013 Google Scholar

[20] X.-Y. J. Wang and J. R. Yuko, "Orion Active Thermal Control System Dynamic Modeling Using Simulink/MATLAB," 48th AIAA Aerospace Sciences Meeting, AIAA 2010-0810, 2010. https://doi.org/10.2514/6.2010-810 Google Scholar

[21] I. S. Khattab, F. Bandarkar, M. Khoubnasabjafari, and A. Jouyban, "Density, viscosity, surface tension, and molar volume of propylene glycol + water mixtures from 293 to 323 K and correlations by the Jouyban-Acree model," Arabian Journal of Chemistry, vol. 10, pp. S71-S75, 2017. https://doi.org/10.1016/j.arabjc.2012.07.012 Google Scholar

[22] N. M. Murthy and S. V. Subrahmanyam, "Ultrasonic behaviour of the system water + propylene glycol," Journal of the Chemical Society, Faraday Transactions 1, vol. 75, pp. 2067-2072, 1979. https://doi.org/10.1039/F19797502067 Google Scholar

[23] X. Ning, K. Xu, Y. Wang, and F. Jiang, "Chang'e-5 complex of lander and ascent vehicle lightweight pumped fluid loop thermal bus: Design and implementation," Acta Aeronautica et Astronautica Sinica, vol. 43, no. 12, Art. no. 126292, 2022. https://doi.org/10.7527/S1000-6893.2021.26292 Google Scholar

## NOMENCLATURE

The symbols used throughout the manuscript are defined below. Subscripts denote reference or base states, model labels, characteristic directions, spatial or temporal indices, or differentiation variables, as appropriate. Derivative subscripts such as $P_X$, $P_\tau$, $P_{XX}$, and $P_{\tau\tau}$ denote partial differentiation and should not be interpreted as ordinary variable indices. Superscripts denote mathematical powers, vector transpose, or discrete time-level indices; in particular, the superscript $n$ denotes a time-step index and not an exponent. An overbar denotes a steady or reference quantity, while bold symbols denote vectors. SI units are used throughout; dimensionless quantities are indicated by "–".

| Mathematical notation | Physical / mathematical meaning | Unit |
|---|---|---|
| $\boldsymbol{\rho}$ | Fluid density | kg $m^{-3}$ |
| $\boldsymbol{\mu}$ | Dynamic viscosity | Pa·s |
| $\mathbf{u}$ | Three-dimensional fluid-velocity vector | m $s^{-1}$ |
| $\boldsymbol{u}$ | Cross-sectionally averaged axial velocity | m $s^{-1}$ |
| $\boldsymbol{p}$ | Instantaneous fluid pressure | Pa |
| $\bar{\boldsymbol{p}}$ | Steady/reference pressure profile | Pa |
| $\mathbf{b}$ | Body-force acceleration vector | m $s^{-2}$ |
| $\boldsymbol{A}$ | Conduit cross-sectional area | $m^2$ |
| $\boldsymbol{x}$ | Dimensional axial coordinate | m |
| $\boldsymbol{t}$ | Dimensional time | s |
| $\boldsymbol{K}$ | Fluid bulk modulus | Pa |
| $\boldsymbol{c}$ | Effective pressure-wave celerity | m $s^{-1}$ |
| $\boldsymbol{L}$ | Equivalent loop length | m |
| $\boldsymbol{D}$ | Hydraulic/internal diameter | m |
| $\boldsymbol{\varepsilon}$ | Absolute internal wall roughness | m |
| $\boldsymbol{\varepsilon/D}$ | Relative wall roughness | - |
| $\boldsymbol{C_{\pm}^{loc}}$ | Local dimensionless nonlinear characteristic speeds | - |
| $\boldsymbol{f_D}$ | Darcy friction factor | - |
| $\boldsymbol{f_0}$ | Darcy friction factor at the steady/base state | - |
| **Re** | Reynolds number | - |
| $\mathbf{Re_0}$ | Steady/base-state Reynolds number | - |
| $\boldsymbol{U_0}$ | Steady reference circulation velocity | m $s^{-1}$ |
| $\boldsymbol{T}$ | Reference fluid temperature | K |
| $\boldsymbol{p_c}$ | Characteristic acoustic pressure scale, $\rho\, cU_0$ | Pa |
| $\boldsymbol{t_c}$ | Acoustic characteristic time, $L/c$ | s |
| $\boldsymbol{T_s}$ | Dimensionless pump-disturbance duration | - |
| $\boldsymbol{t_s}$ | Physical pump-disturbance duration, $T_s\, t_c$ | s |

| Mathematical notation | Physical / mathematical meaning | Unit |
|---|---|---|
| $\boldsymbol{\Delta p_{\mathrm{NL}}}$ | Nonlinear-model transient pressure excursion | Pa |
| $\boldsymbol{P}$ | Dimensionless pressure perturbation | - |
| $\boldsymbol{V}$ | Dimensionless velocity perturbation | - |
| $\boldsymbol{X}$ | Dimensionless axial coordinate, $x/L$ | - |
| $\boldsymbol{\tau}$ | Dimensionless time, $ct/L$ | - |
| $\boldsymbol{M}$ | Acoustic Mach number, $U_0/c$ | - |
| $\boldsymbol{\Gamma}$ | Dimensionless turbulent-friction parameter | - |
| $\boldsymbol{\varepsilon_b}$ | Dimensionless steady-pressure-gradient parameter | - |
| $\boldsymbol{\Lambda_L}$ | Dimensionless laminar damping coefficient | - |
| $\boldsymbol{\lambda}$ | Generic dimensionless linear damping coefficient | - |
| $\boldsymbol{S(X,\tau)}$ | Dimensionless localized pump/control source | - |
| $\boldsymbol{A_s}$ | Dimensionless pump-disturbance amplitude | - |
| $\boldsymbol{\chi_p(X)}$ | Normalized spatial pump kernel | - |
| $\boldsymbol{h(\tau)}$ | Dimensionless temporal forcing function | - |
| $\boldsymbol{D_M}$ | Derivative following the steady circulation | - |
| $\boldsymbol{C_+}$ | Positive dimensionless characteristic speed | - |
| $\boldsymbol{C_-}$ | Negative dimensionless characteristic speed | - |
| $\boldsymbol{c_+}$ | Dimensional downstream characteristic speed | m $s^{-1}$ |
| $\boldsymbol{c_-}$ | Dimensional upstream characteristic speed | m $s^{-1}$ |
| $\boldsymbol{N}$ | Number of computational grid nodes | - |
| $\boldsymbol{j}$ | Spatial-node index | - |
| $\boldsymbol{n}$ | Time-step index | - |
| $\boldsymbol{\Delta X}$ | Dimensionless grid spacing | - |
| $\boldsymbol{\Delta\tau}$ | Dimensionless time step | - |

| Mathematical notation | Physical / mathematical meaning | Unit |
|---|---|---|
| $\phi_j$ | Generic numerical field at spatial node j | - |
| $Q$ | Complete semi-discrete state vector | - |
| $Q^n$ | State vector at time step n | - |
| $Q^{n+1}$ | State vector at the next time step | - |
| $Q^{\mathrm{T}}$ | Transpose of the state vector | - |
| $R(Q,\tau)$ | Semi-discrete right-hand-side operator | - |
| $k_1$ | First Runge-Kutta stage | - |
| $k_2$ | Second Runge-Kutta stage | - |
| $k_3$ | Third Runge-Kutta stage | - |
| $k_4$ | Fourth Runge-Kutta stage | - |
| $C_{\mathrm{CFL}}$ | Courant/CFL number | - |
| $E_{P,2}$ | Global pressure-field discrepancy | % |
| $E_{P,\max}$ | Relative peak-pressure discrepancy | % |
| $E_t$ | Relative timing discrepancy | % |
| $r_{\mathrm{obs}}$ | Observed numerical convergence order | - |
| $q$ | Scalar nonlinear travelling-wave benchmark variable | - |
| $q_0$ | Initial travelling-wave benchmark field | - |
| $A_q$ | Benchmark-wave amplitude | - |
| $\xi$ | Characteristic/Lagrangian coordinate | - |
| $\tau_s$ | Characteristic steepening time | - |
| $\tau_f$ | Final dimensionless benchmark time | - |
| $e_N$ | Relative numerical error on an N-node grid | - |
| $P_N$ | Numerical pressure solution on grid N | - |
| $P_{\mathrm{exact}}$ | Exact/reference pressure solution | - |
| $P^n_{\mathrm{NL},j}$ | Nonlinear pressure at node j and time step n | - |
| $P^n_{L,j}$ | Linear pressure at node j and time step n | - |
| $P_{\max,\mathrm{NL}}$ | Maximum nonlinear pressure response | - |
| $P_{\max,L}$ | Maximum linear pressure response | - |
| $\tau_{\max,\mathrm{NL}}$ | Time of nonlinear pressure maximum | - |
| $\tau_{\max,L}$ | Time of linear pressure maximum | - |
| $P_X$ | First derivative of P with respect to X | - |
| $P_\tau$ | First derivative of P with respect to tau | - |
| $P_{XX}$ | Second derivative of P with respect to X | - |
| $P_{\tau\tau}$ | Second derivative of P with respect to tau | - |
| $V_X$ | First derivative of V with respect to X | - |
| $V_\tau$ | First derivative of V with respect to tau | - |
| $\nabla$ | Gradient differential operator | $m^{-1}$ |
| $\nabla^2$ | Laplacian operator | $m^{-2}$ |
| $R$ | Restriction operator used to map a fine-grid solution to coincident nodes of the next coarser grid | – |